Land–Snow–Waterbody 2-Endmember-Mixed-Pixel Effect on the Measurement Error of the Moon-Based Earth Radiation Observatory

Wentao Duan, Shuanggen Jin, *Senior Member, IEEE*, and Weixun Zhou, *Member, IEEE*

***Abstract*— The Moon-based Earth Radiation Observatory (MERO) has the potential to complement current Earth Radiation Budget (ERB) missions by providing higher temporal resolution data, especially for the Earth's polar regions. Regarding the MERO mission design, quantifying its mixed-pixel-induced uncertainty is crucial, which occupies an important part in the MERO inherent systematic errors. However, current knowledge about this MERO mixed-pixel-induced uncertainty is still limited. In this study, we proposed a MERO 2-endmember-mixed-pixel error quantification method and explored such errors in the land–snow, land–waterbody, and waterbody–snow mixing scenarios. Results indicate that the land–snow mixing leads to the biggest measurement errors, which are as large as 4.02% and 7.98% for the Earth's top of the atmosphere (TOA) outgoing solar-reflected shortwave radiation (OSR) and outgoing thermally emitted longwave radiation (OLR) fluxes, respectively. The waterbody–snow mixing caused the second largest measurement error with a TOA OSR maximum of 3.01% and TOA OLR maximum of 7.08%. The land–waterbody mixing results in the least measurement error with a TOA OSR maximum of 0.79% and a TOA OLR maximum of 0.41%.**

***Index Terms*— Mixed-pixel error, Moon-based Earth Radiation Observatory (MERO), outgoing solar-reflected shortwave radiation (OSR), outgoing thermally emitted longwave radiation (OLR).**

I. Introduction

THE imbalance in the Earth's Radiation Budget (ERB) is one of the dominant factors that drive the global climate change. This Earth radiation imbalance (ERI) is determined by the difference between the incoming solar radiation [total solar irradiance (TSI)] and the Earth's outgoing radiation (EOR) at the top of the atmosphere (TOA). The EOR is comprised of two parts: the outgoing solar-reflected shortwave radiation (OSR) and the outgoing thermally emitted longwave radiation (OLR). Since the sun is a relatively stable radiation source, current TSI measurement has a relatively high precision with the help of continuous TSI observations since the 1970s, such as the Solar Radiation & Climate Experiment (SORCE) [1]. A recent study reported that the TSI is estimated to be 1362.0 + 0.9 W/m^2 by comparison of the independent TSI measurements [2]. In contrast, measuring the TOA OSR and OLR is more challengeable due to the high temporal-spatial variability of the TOA OSR and OLR. So far, several satellite-based ERB missions have been deployed for the Earth TOA OSR and OLR observations, such as the Earth Radiation Budget Experiment (ERBE), the Cloud and Earth's Radiant Energy System (CERES), the Geostationary Earth Radiation Budget (GERB). Studies based on these TSI, OSR, and OLR measurements indicated that the average absolute value of ERI in recent centuries approximated 1 W/m^2 [3]. These satellite-based ERB observations had indeed deepened our understanding of how the ERI drives the climate change [4]. However, current satellite-based OSR and OLR measurements have evident uncertainty, partially due to the limited temporal sampling frequency and the non-simultaneous sampling of the global TOA OSR and OLR spatial-temporal variability [5], [6], [7].

As a next-generation ERB mission, a Moon-based Earth Radiation Observatory (MERO) could bring several improvements to current ERB observations, which are detailly shown hereafter. 1) Compared to current low-Earth-orbit (LEO) ERB missions, the MERO could provide much larger temporal sampling coverage. The MERO could continuously observe a certain region on Earth for about 12 h per day, producing nearly 48 temporal samples for one Earth place in a diurnal cycle if the sampling interval is set as 15 min (the sampling interval of the GERB), which is about 24 times larger than that of a single LEO ERB satellite. These abundant temporal samples could help to reveal the small-time-scale TOA OSR and OLR variations more precisely. 2) A MERO could instantaneously observe the whole Earth disk without the sampling bias caused by the non-simultaneous sampling, benefiting deriving the regional and global radiation imbalance

Manuscript received 2 August 2022; revised 7 November 2022; accepted 29 November 2022. Date of publication 2 December 2022; date of current version 15 December 2022. This work was supported in part by the Qian Xuesen Laboratory, China Academy of Space Technology through the Experiments for Space Exploration Program under Grant TKTSPY-2020-06-02; in part by the Project funded by China Postdoctoral Science Foundation under Grant 2022M711668; and in part by the Natural Science Foundation, Jiangsu Higher Education Institutions of China, under Grant 22KJB420003. *(Corresponding author: Shuanggen Jin.)*

Wentao Duan is with the Joint International Research Laboratory of Climate and Environment Change (ILCEC), Nanjing University of Information Science and Technology, Nanjing 210044, China (e-mail: eilen4011@nuist.edu.cn).

Shuanggen Jin is with the School of Remote Sensing and Geomatics Engineering, Nanjing University of Information Science and Technology, Nanjing 210044, China, also with the Shanghai Astronomical Observatory, Chinese Academy of Sciences (CAS), Shanghai 200030, China, and also with the School of Surveying and Land Information Engineering, Henan Polytechnic University, Jiaozuo 454000, China (e-mail: sgjin@shao.ac.cn).

Weixun Zhou is with the School of Remote Sensing and Geomatics Engineering, Nanjing University of Information Science and Technology, Nanjing 210044, China (e-mail: zhouwx@nuist.edu.cn).

Digital Object Identifier 10.1109/LGRS.2022.3226499

TABLE I
ENDMEMBERS USED IN THE MIXING SCENARIO CONSTRUCTION

Endmembers	True TOA OSR flux (W/m^2)	True TOA OLR flux (W/m^2)	Surface type	Cloud fraction (%)	Optical depth	Cloud emissivity	Vertical temperature change (K)	Cloud phase	Precipitable water (cm)	Surface skin temperature (K)
Land OSR-OLR scene type	94.69	235.19	Land	66.50	3.34	0.77	28.93	1.46	2.26	286.43
Snow OSR-OLR scene type	112.87	167.47	Snow	61.18	4.46	0.84	7.44	1.76	0.27	242.92
Waterbody OSR-OLR scene type	98.48	231.15	Water body	70.60	3.76	0.79	25.57	1.41	2.04	283.75

with less uncertainty. 3) Current LEO ERB missions can hardly provide high temporal resolution observations for the OSR and OLR variations of polar regions that are vital for understanding the energy budget of Arctica and Antarctica in the transition periods (the melting and frozen periods). Besides, the in-orbit geostationary-Earth-orbit (GEO) ERB mission could just provide very oblique observations for polar regions, which precludes producing ERB data with satisfied accuracy. In comparison, a MERO located on the near surface of the Moon (90°E–90°W) could simultaneously observe more than 45% of the Arctic/Antarctic region during 50% of a lunar orbital period (27.3 days) with an acceptable obliquity. This enables a MERO to provide higher temporal resolution Arctic/Antarctic TOA OSR and OLR data than an LEO counterpart to facilitate better capturing the small-temporal-scale OSR and OLR variability in Earth's polar regions. 4) Since the Earth distance (380 000 km on average) is much larger than the Moon's radius (1737 km on average), nearly all locations on the Moon's near surface (90°E–90°W) share a highly similar Earth-viewing geometry, which could facilitate data merging of multiple MERO missions located differently on the near surface of the Moon [8].

The core task of a MERO is to observe the regional TOA OSR and OLR fluxes with high temporal sampling coverage. Currently, The MERO system is conceptually designed as a non-scanner imaging spectroradiometer. Every detector observes a certain region on Earth, which is represented by the corresponding pixel. The work process of a MERO system is briefly depicted as follows: 1) Earth TOA OSR and OLR of one pixel pass through the Earth-Moon space, then they are captured and converted to the electrical signal by the corresponding unit of the detector array; 2) such a signal is then processed to the digital number (DN) by the readout integrated circuit (ROIC); and 3) finally, a measurement TOA OSR/OLR flux of the pixel value could be derived through the radiometric calibration and Earth TOA radiative anisotropic factors. As indicated above, the whole region that the pixel covers, is assumed to be uniform in the TOA OSR/OLR, which is denoted by the produced TOA OSR/OLR flux value of the corresponding pixel. However, this uniform pixel value will neglect the actual spatial variability of the TOA OSR/OLR in the pixel, which would bring certain uncertainties in the TOA OSR/OLR data product. In fact, this spatial variability is substantially influenced by the mixed situation of the TOA OSR/OLR scene types in the pixel. A TOA OSR/OLR scene type is the combination of the factors that affects the TOA OSR/OLR flux, different OSR/OLR scene type, therefore, has distinct OSR/OLR flux [9], [10]. Accordingly, the pixel mixed condition of the TOA OSR/OLR scene type would have obvious consequences on the measurement uncertainty of the MERO OSR/OLR data (the difference between the uniform pixel OSR/OLR flux and the actual OSR/OLR spatial variability in the pixel), which is the important part of the MERO inherent systematic error. However, current knowledge about this mixed-pixel-induced error of a MERO is still limited.

The objective of this study is to reveal the MERO OSR/OLR measurement errors induced by three OSR/OLR 2-endmember-mixed scenarios (land-based, ocean-based, and snow-based), respectively, which could facilitate the MERO systematic uncertainty (error) evaluation. This letter is constructed as follows. Section II mainly describes the TOA OSR/OLR mixing scenarios in one pixel that is considered in this study. Section III focuses on the MERO 2-endmember-mixed-pixel error quantification method. Section IV exhibits the primary results and discussions. Section V presents the main conclusions.

II. TOA OSR/OLR MIXING SCENARIOS IN ONE PIXEL

Endmembers for the mixing scenario construction are shown in Table I. A scene type is the combination of the primary factors that dominate the TOA OSR/OLR angular-dependent radiance, including the surface type, the related cloud, and meteorological parameters (such as the optical depth and the cloud fraction). Besides, we also give the "true" TOA OSR/OLR flux for each endmember to evaluate the measurement error. Values of the true OSR/OLR flux and the factors (such as optical depth and the cloud fraction) are determined by annually averaging the CERES SYN dataset of 2020. For example, cloud fraction of the land OSR-OLR scene type is derived by averaging all cloud fraction data with land surface type through the year 2020. Note that the OSR-OLR scene type used in this study is the combination of the original OSR and OLR scene types, which could be used for both the TOA OSR and OLR mixed-pixel-induced error estimations. The surface type used in this study includes three categories: land, snow, and waterbody. Their correspondence to the standard International Geosphere-Biosphere Program

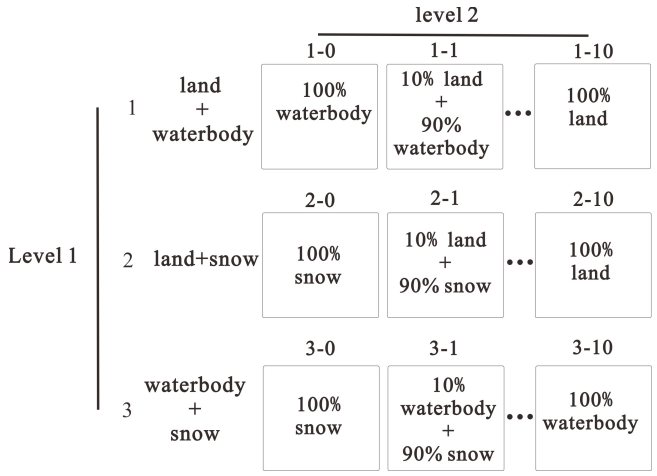

Fig. 1. TOA OSR/OLR pixel mixing scenarios. Level 1 aims at the endmember category mixing and level 2 focuses on the endmember proportion structure.

(IGBP) surface type is set as follows: the water body used in this study corresponds to the water bodies type in IGBP, the snow type in this study corresponds to the snow and ice type in IGBP, land type in our study corresponds to the other IGBP types except for the tundra type. The TOA OSR/OLR scene-type mixing scenarios in one pixel are constructed by two levels. Level 1 aims at the endmember category mixing (land + waterbody mixing, land + snow mixing, and waterbody + snow mixing). Level 2 concentrates on the endmember proportion structure (see Fig. 1). For example, in the land + waterbody mixing circumstance, the specific 11 mixing scenarios (1–0 to 1–10) are produced by the land proportion augmented with the increasing step of 10% (Fig. 1).

III. MERO 2-Endmember-Mixed-Pixel Error Quantification Method

The MERO 2-endmember-mixed-pixel-induced measurement error ($\mathrm{Err_{mx}}$) could be derived through the difference between the true value of every mixed endmember and the simulated MERO-produced pixel value

$$\mathrm{Err}^k_{\mathrm{mx}} = \frac{1}{pn}\sum_{p=1}^{pn}\frac{1}{t}\sum_{i=1}^{t}\frac{\sqrt{\left(M^k_{p,i}-T^k_1\right)^2+\left(M^k_{p,i}-T^k_2\right)^2}}{\left(T^k_1+T^k_2\right)} \quad k=\mathrm{OSR\ or\ OLR} \tag{1}$$

where T_1 and T_2 are the true TOA fluxes (OSR or OLR) of the endmembers 1 and 2 mixed in the pixel, respectively. $M_{p,i}$ is the simulated pixel value of TOA flux (OSR or OLR) of pixel p at time i [detailed derivation of $M_{p,i}$ is illustrated in (2)]. t in (1) is the amount of all the time points in 2020 (time step is 1 h), and the measurement error is calculated as the temporal average value due to the time-dependent MERO-Earth geometry would have consequences for $M_{p,i}$. After the temporally averaging, a pixel averaging is conducted due to that different pixels differ in their $M_{p,i}$ (pn is the amounts of the pixels on the focal plane array of the MERO). $M_{p,i}$ of a certain pixel at a certain time could be derived through

$$M^k = \frac{\iint_S F^k D^{-2} W^k \cos\upsilon\cos\omega ds}{W^k_S D^{-2}_S \cos\upsilon_S \cos\omega_S A_s}, \quad k=\mathrm{OSR\ or\ OLR} \tag{2}$$

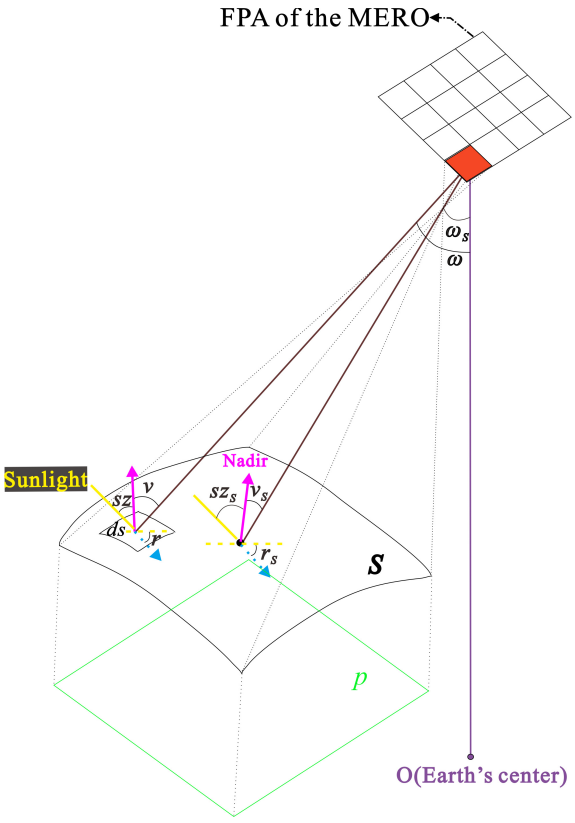

Fig. 2. 1) Observing mechanism of an MERO. The whole focal plane array (assemble of multiple detector units, abbreviated as FPA) of the MERO system would instantaneously "photograph" the whole TOA Earth disk. Specifically, one detector unit (the red rectangle on the upper right) would just "photograph" part of the full TOA Earth disk (S), which can be represented by a pixel p (projection of S on the FPA plane). 2) Geometric parameters describing the MERO observing mechanism. Geometric parameters for a differential area (ds) in S: the solar zenith angle (sz), the viewing zenith angle (υ), the relative azimuth angle (r), and Earth center zenith angle (ω). Geometric parameters for the whole S are defined by the similar way using the center of the S, such as the solar zenith angle (sz_S), the viewing zenith angle (υ_S), the relative azimuth angle (r_S), and Earth center zenith angle (ω_S).

where S is the Earth TOA area that a pixel represents (100 × 100 km at the equator region). F is the true TOA OSR/OLR flux of the differential area (ds) within the pixel, which is given by the endmember type of ds (see Table I). D is the distance between the MERO site and the differential area ds; D_S is the MERO-whole-pixel distance, which is defined as the distance between the MERO site and the center of S (see Fig. 2). υ is the viewing zenith angle of the MERO sensor toward ds; υ_S is the MERO-whole-pixel viewing zenith angle (similar to D_S), which is defined as the viewing zenith angle of the MERO site toward the center of S. ω denotes the angler between the Earth's center viewing vector and the differential area (ds) viewing vector; ω_S is the angle between the Earth's center viewing vector and the S-center viewing vector (similar to the definitions of υ_S and D_S). Visualizations of D, D_S, υ, υ_S, ω, and ω_S are illustrated in Fig. 2; all these parameters can be derived by utilizing the MERO-Earth geometric method proposed in our previous study [11], [12]. W is the TOA OSR/OLR anisotropic factor of the differential area (ds), which is the ratio of the TOA OSR/OLR flux and the directional radiance. W is a

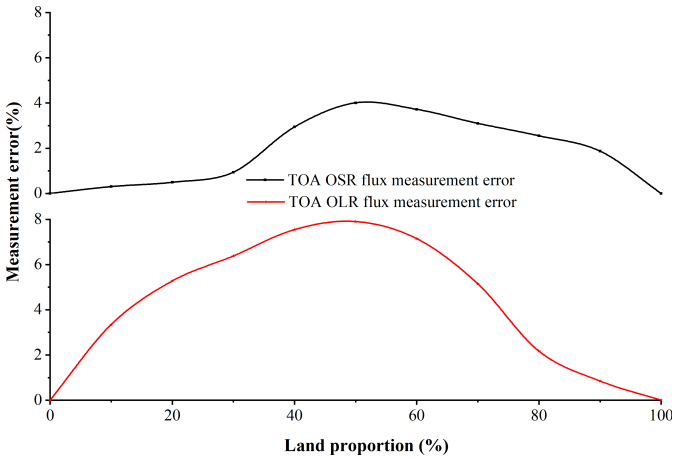

Fig. 3. MERO measurement errors in the land–snow mixed pixel at different endmember proportional structures.

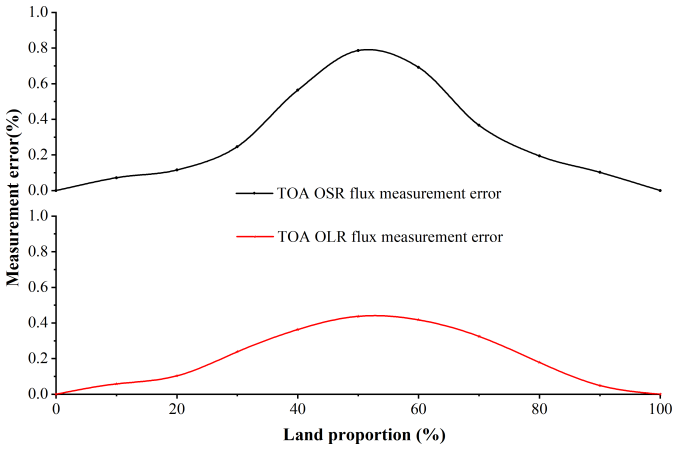

Fig. 4. MERO measurement errors in the land–waterbody mixed pixel at different endmember proportional structures.

highly spatial-temporal-dependent variable, which is closely related to the type of the surface beneath the TOA area, the cloud and meteorological parameters (such as optical depth and cloud fraction) and the viewing geometry (such as the viewing zenith angle and the relative azimuth angle). Here, we used the Earth-TOA-MERO radiant anisotropy method proposed in our recently published study based on the CERES Angular Distribution Models (ADMs) to generate W with full consideration of its dependence on the related parameters mentioned above [12]. W_S in (2) is the integrated OSR/OLR anisotropic factor of the whole pixel area S, which could be derived through the area weighting integration of W within S

$$W_S^k = \frac{\iint_S W^k ds}{A_S}, \quad k = \text{OSR or OLR} \tag{3}$$

where A_S is the area size of S.

IV. Results and Discussion

A. Measurement Error in Land–Snow Mixed Pixel

The measurement errors in the land–snow mixed pixel at various endmember proportional structures are shown in Fig. 3. It is indicated that the overall measurement error of TOA OLR is generally about two times larger than that of TOA OSR in the land–snow mixed scenario. This is due to that the TOA OLR flux difference between the land and snow endmembers (67.72 W/m^2, see Table I) is evidently larger than that of the TOA OSR flux (18.18 W/m^2), which makes four times larger numerator in (1) of OLR than that of OSR, whereas the OLR denominator is about two times larger than that of OSR (Table I). The measurement error would be positively correlated with the mixing extent of the pixel since the measurement error reflects the general deviation between the pixel measurement and the true values of endmembers [see (1)]. For example, when the land proportion is 0% or 100% (the purified snow or land pixel), the mixed extent of the pixel would be the least, making the pixel OSR/OLR flux measurement definitely equal to the OSR/OLR true value of the only endmember, in other words, the OSR/OLR measurement error approximates 0 (Fig. 3). When the mixed extent reaches the maximum (50% land and 50% snow mixed), the deviation between the pixel OSR/OLR measurement and the two endmember OSR/OLR true flux values approximates the maximum [see (1)], leading to the maximum measurement errors (about 4.02% for TOA OSR flux and 7.98% for TOA OLR flux, see Fig. 3).

B. Measurement Error in Land–Waterbody Mixed Pixel

The measurement errors in the land–waterbody mixed pixel at various endmember proportional structures are exhibited in Fig. 4. It is shown that the maximum measurement errors of TOA OSR and OLR fluxes are 0.79% and 0.41%, respectively. Both the maximum OSR and OLR measurement errors occur at the case where the mixed extent is largest (50% land and 50% snow mixed). In the land–waterbody mixed pixel, the TOA OSR flux measurement error is generally larger than that of TOA OLR flux at the same mixing extent though the TOA OSR flux difference (3.79 W/m^2) between the land and waterbody endmembers is not much less than that of TOA OLR flux (4.04 W/m^2). This is due to that the TOA OLR flux of either of the land or waterbody endmember is about two times larger than that of TOA OSR flux, resulting in two times larger denominator in (1) of TOA OLR than that of TOA OSR whereas their numerators have much less difference.

C. Measurement Error in Waterbody–Snow Mixed Pixel

The MERO measurement errors in the waterbody–snow mixed pixel at various endmember mixing structures are shown in Fig. 5. It is indicated that the maximum error for TOA OSR and OLR flux measurements approximate 3.01% and 7.08%, respectively, which also occurs at the largest mixing extent (50% waterbody and 50% snow mixed). In the waterbody–snow mixed pixel, the TOA OLR flux measurement error is generally over two times larger than that of TOA OSR flux at the same mixing extent. This is primarily attributed to that the TOA OLR flux difference between the waterbody and snow endmembers (63.68 W/m^2, see Table I) is evidently bigger than that of the TOA OSR flux (14.39 W/m^2), which makes a nearly four times larger numerator in (1) of OLR than that of OSR, whereas the OLR denominator is about two times larger than that of OSR (Table I).

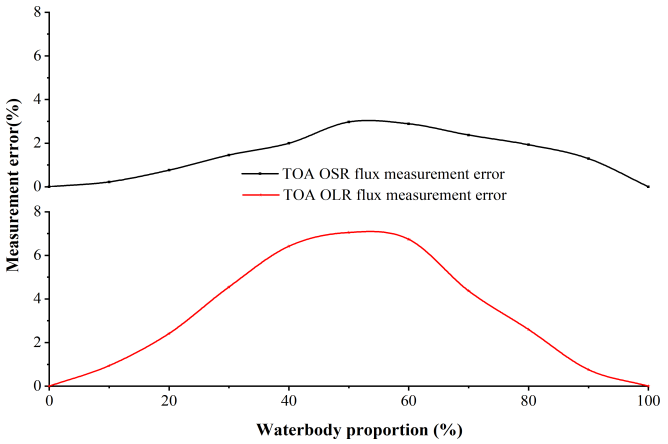

Fig. 5. MERO measurement errors in the waterbody–snow mixed pixel at different endmember proportional structures.

D. Comparison of Three Mixing Scenarios

As indicated above, the land–snow mixing in a pixel could lead to the maximum measurement errors as large as 4.02% and 7.98% for Earth TOA OSR and OLR fluxes, respectively. In comparison, the waterbody–snow mixing caused the second largest measurement error (OSR maximum: 3.01% and OLR maximum: 7.08%). While the land–waterbody mixing results in the least measurement error (OSR maximum: 0.79% and OLR maximum: 0.41%). We consider this ranking to be caused by the true TOA fluxes of the two endmembers and their difference; a larger difference would result in bigger deviation between the simulated OSR/OLR observed pixel value and the true OSR/OLR values of the two endmembers, leading to larger mixing pixel error [see (1)]. For example, either the TOA OSR or OLR flux measurement error in the land–waterbody mixed pixel (maximum values are 0.79% and 0.41% for TOA OSR and OLR flux, respectively) is much smaller than that in the land–snow mixed pixel (maximum of 4.02% for OSR and maximum of 7.98% for OLR); this is primarily due to that either of the TOA OSR or OLR flux difference between the land and waterbody endmembers (OSR: 3.79 W/m^2 and OLR: 4.04 W/m^2) are much smaller than that between the land and snow endmembers (OSR: 18.18 W/m^2 and OLR: 67.72 W/m^2).

In this letter, we adopted an unchanged true TOA flux and the TOA-anisotropy-factor-dominant factors to reveal the general measurement errors caused by the land–snow, land–waterbody, and waterbody–snow mixing scenarios, respectively. However, such an assumption would neglect the influences from the temporal variations of these factors, which may bring certain uncertainties to the simulation results. Besides, as the initial stage, we just categorize the surface type as land, waterbody, and snow, which is far away from the IGBP classifications that used 19 types to describe the Earth's surface. These insufficiencies are expected to be complemented in our future studies.

V. Conclusion

The MERO, which acts as a next-generation Earth radiation budget (ERB) observing system, could complement current ERB observations by providing higher temporal resolution data. The MERO mixed-pixel-induced uncertainty plays an important role in the MERO inherently systematic error. In this study, a quantifying method of MERO 2-endmember-mixed-pixel error is proposed and such errors in the land–snow, land–waterbody, and waterbody–snow mixing scenarios are investigated. Results show that the land–snow mixing in a pixel could lead to the maximum measurement errors, which are as large as 4.02% and 7.98% for Earth TOA OSR and OLR fluxes, respectively. In comparison, the waterbody–snow mixing caused the second largest measurement error (OSR maximum: 3.01% and OLR maximum: 7.08%), whereas the land–waterbody mixing yields the least measurement error (OSR maximum: 0.79% and OLR maximum: 0.41%).

References

[1] G. Kopp and J. L. Lean, "A new, lower value of total solar irradiance: Evidence and climate significance," *Geophys. Res. Lett.*, vol. 38, no. 1, pp. 1–7, Jan. 2011, doi: 10.1029/2010GL045777.

[2] S. Dewitte and N. Clerbaux, "Measurement of the Earth radiation budget at the top of the atmosphere—A review," *Remote Sens.*, vol. 9, no. 11, p. 1143, Nov. 2017. [Online]. Available: https://www.mdpi.com/2072-4292/9/11/1143

[3] K. Von Schuckmann et al., "An imperative to monitor Earth's energy imbalance," *Nature Climate Change*, vol. 6, no. 2, pp. 138–154, 2016, doi: 10.1038/NCLIMATE2876.

[4] N. G. Loeb et al., "Clouds and the Earth's Radiant Energy System (CERES) energy balanced and filled (EBAF) top-of-atmosphere (TOA) edition-4.0 data product," *J. Climate*, vol. 31, no. 2, pp. 895–918, 2018, doi: 10.1175/jcli-d-17-0208.1.

[5] G. L. Smith, T. Wong, and K. A. Bush, "Time-sampling errors of Earth radiation from satellites: Theory for outgoing longwave radiation," *IEEE Trans. Geosci. Remote Sens.*, vol. 53, no. 3, pp. 1656–1665, Mar. 2015, doi: 10.1109/TGRS.2014.2338793.

[6] G. L. Smith and T. Wong, "Time-sampling errors of Earth radiation from satellites: Theory for monthly mean albedo," *IEEE Trans. Geosci. Remote Sens.*, vol. 54, no. 6, pp. 3107–3115, Jun. 2016, doi: 10.1109/TGRS.2015.2503982.

[7] M. Meftah et al., "UVSQ-SAT, a Pathfinder CubeSat mission for observing essential climate variables," *Remote Sens.*, vol. 12, no. 1, p. 92, 2020. [Online]. Available: https://www.mdpi.com/2072-4292/12/1/92

[8] W. Duan, S. Huang, and C. Nie, "Conceptual design of a Moon-based Earth radiation observatory," *Int. J. Remote Sens.*, vol. 39, no. 18, pp. 5834–5849, Sep. 2018, doi: 10.1080/01431161.2018.1512770.

[9] N. G. Loeb, S. Kato, K. Loukachine, and N. Manalosmith, "Angular distribution models for top-of-atmosphere radiative flux estimation from the Clouds and the Earth's Radiant Energy System instrument on the Terra satellite. Part I: Methodology," *J. Atmos. Ocean. Technol.*, vol. 22, no. 4, pp. 338–351, 2005, doi: 10.1175/JTECH1712.1.

[10] W. Su, J. Corbett, Z. Eitzen, and L. Liang, "Next-generation angular distribution models for top-of-atmosphere radiative flux calculation from CERES instruments: Methodology," *Atmos. Meas. Techn.*, vol. 8, no. 2, pp. 611–632, Feb. 2015, doi: 10.5194/amt-8-611-2015.

[11] W. Duan, S. Huang, and C. Nie, "Entrance pupil irradiance estimating model for a Moon-based Earth radiation observatory instrument," *Remote Sens.*, vol. 11, no. 5, p. 583, Mar. 2019, doi: 10.3390/rs11050583.

[12] W. Duan and S. Jin, "An improved methodology for quantifying pixel-scale entrance pupil irradiance of a moon-based Earth radiation observatory," *ISPRS J. Photogramm. Remote Sens.*, vol. 183, pp. 389–402, Jan. 2022, doi: 10.1016/j.isprsjprs.2021.11.019.